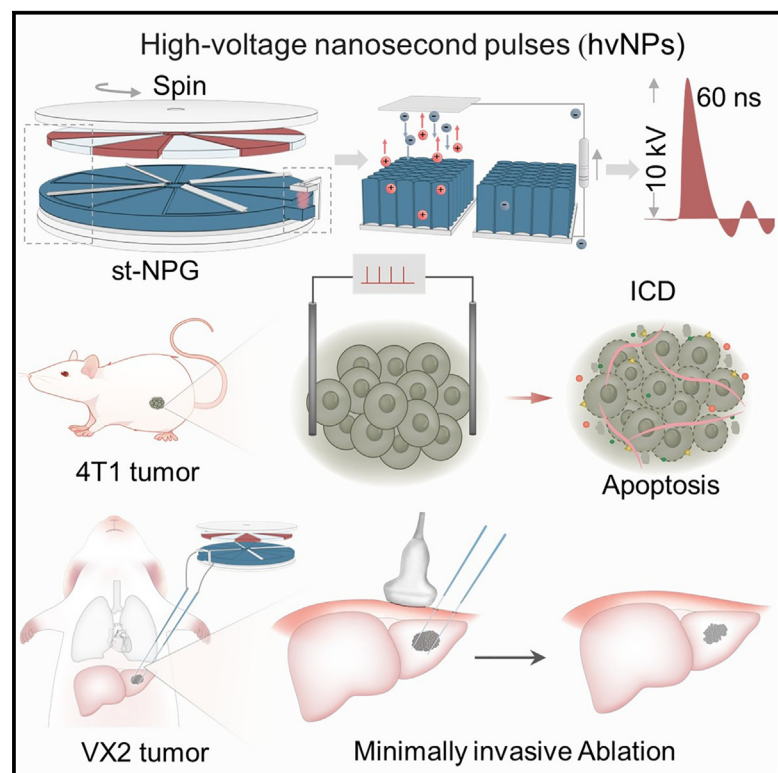


# Schottky nanodiodes array enabled triboelectric nanosecond pulse generator for ultralow-cost tumor therapy

## Graphical abstract



## Highlights

- Developed a mechanical energy-driven high-voltage nanosecond pulse generator
- $\text{TiO}_2$  nanotubes and Ti form Schottky diodes for efficient charge separation
- The system can generate a 10 kV voltage with a 60 ns pulse width
- st-NPG shows effective tumor ablation and excellent biosafety in animal models

## Authors

Lingling Xu, Engui Wang, Yong Kang, ..., Han Ouyang, Chunying Chen, Zhou Li

## Correspondence

ouyanghan@ucas.ac.cn (H.O.),  
chenchy@nanoctr.cn (C.C.),  
zli@binn.cas.cn (Z.L.)

## In brief

This study introduces a cost-effective, mechanical-energy-driven high-voltage nanosecond pulse generator (st-NPG) that eliminates the need for external power sources or complex circuits. Utilizing Schottky nanodiode arrays and the triboelectric effect, the device efficiently generates stable high-voltage pulses and has been successfully applied in subcutaneous tumor treatment in mice and *in situ* liver cancer ablation in rabbits, with minimal damage to healthy tissue. The st-NPG has broad applications in biomedical, environmental, and industrial fields, offering a sustainable, accessible solution for resource-constrained regions.



**Develop**

Prototype with demonstrated applications in relevant environment

Xu et al., 2025, Device 3, 100721  
June 20, 2025 © 2025 The Author(s). Published by Elsevier Inc.  
<https://doi.org/10.1016/j.device.2025.100721>

CellPress

Article

# Schottky nanodiodes array enabled triboelectric nanosecond pulse generator for ultralow-cost tumor therapy

Lingling Xu,<sup>1,3,7</sup> Engui Wang,<sup>2,3,7</sup> Yong Kang,<sup>5,7</sup> Dianxun Fu,<sup>6,7</sup> Lin Luo,<sup>3</sup> Yichang Quan,<sup>2</sup> Yuan Xi,<sup>2</sup> Jing Huang,<sup>2,3</sup> Xi Cui,<sup>2</sup> Jia Zeng,<sup>6</sup> Dongjie Jiang,<sup>2</sup> Bojing Shi,<sup>2</sup> Hongqing Feng,<sup>3</sup> Han Ouyang,<sup>3,\*</sup> Chunying Chen,<sup>1,\*</sup> and Zhou Li<sup>2,3,4,8,\*</sup>

<sup>1</sup>New Cornerstone Science Laboratory, CAS Key Laboratory for Biomedical Effects of Nanomaterials and Nanosafety and CAS Center for Excellence in Nanoscience, National Center for Nanoscience and Technology, Beijing 100190, China

<sup>2</sup>Beijing Key Laboratory of Micro-nano Energy and Sensor, Beijing Institute of Nanoenergy and Nanosystems, Chinese Academy of Sciences, Beijing 101400, China

<sup>3</sup>School of Nanoscience and Engineering, University of Chinese Academy of Sciences, Beijing 100049, China

<sup>4</sup>Tsinghua Changgung Hospital, School of Clinical Medicine, School of Biomedical Engineering, Tsinghua Medicine, Tsinghua University, Beijing 100084, China

<sup>5</sup>Academy of Medical Engineering and Translational Medicine Medical College, Tianjin University, Tianjin 300072, China

<sup>6</sup>Department of Radiology, Tianjin Key Laboratory of Functional Imaging, Tianjin Medical University General Hospital, Tianjin 300052, China

<sup>7</sup>These authors contributed equally

<sup>8</sup>Lead contact

\*Correspondence: [ouyanghan@ucas.ac.cn](mailto:ouyanghan@ucas.ac.cn) (H.O.), [chenchy@nanoctr.cn](mailto:chenchy@nanoctr.cn) (C.C.), [zli@binn.cas.cn](mailto:zli@binn.cas.cn) (Z.L.)

<https://doi.org/10.1016/j.device.2025.100721>

**THE BIGGER PICTURE** High-voltage nanosecond pulses have significant potential in biomedicine and materials science, enabling precise reactions in cells and tissues. However, current pulse generators are costly due to complex power systems and circuits. This study introduces a low-cost, mechanical-energy-driven high-voltage pulse generator (Schottky nanodiode array-enabled triboelectric nanosecond pulse generator [st-NPG]) based on the triboelectric effect and Schottky diode arrays. Using titanium dioxide nanotube arrays and titanium electrodes, the st-NPG enhances charge separation and storage, generating efficient pulses. By eliminating external power sources, the st-NPG lowers costs and increases accessibility, especially in resource-limited areas. Demonstrating effective tumor ablation with minimal tissue damage, the st-NPG provides a sustainable solution with wide-reaching potential in healthcare, environmental protection, and industry.

## SUMMARY

Generating reliable high-voltage nanosecond pulses (hvNPs) is challenging in terms of materials, electronics, and power supply. Inspired by the natural phenomenon of lightning, we report a Schottky nanodiode array-enabled triboelectric nanosecond pulse generator (st-NPG) that eliminates the need for an external electrical power supply or boosting circuits, relying instead on mechanical energy input to directly generate hvNPs. This st-NPG, with high voltage (10 kV), peak power (17 MW), single-pulse energy (0.6 J), and stability (7 days of operation), is enabled by a capacitive wafer-scale semiconductor titanium dioxide (TiO<sub>2</sub>) nanotube array with substantial charge storage and trapping capabilities. The st-NPG also enabled pulsed ablation for tumor treatment in mice and rabbits via minimally invasive interventional surgery. The ultracheap (<1/1,000 of commercial cost), power-source-free st-NPG should open opportunities for healthcare, environmental protection, science, and education applications around the world, especially in resource-poor regions.

## INTRODUCTION

High-voltage nanosecond pulses (hvNPs) are based on pulsed power, which accumulates electric energy and releases it in nanosecond bursts, producing high-power electric pulses.<sup>1</sup> It can

induce precise and controlled nanoscale reactions in cells, biological tissues, and materials, leading to their destruction or modification. In the field of biomedical sciences, nanosecond pulses not only cause cell membrane perforation but can also penetrate the membrane to directly affect the intracellular components,

leading to effects such as organelle membrane perforation, cytoskeletal depolymerization, intracellular calcium ion release, and DNA damage.<sup>2,3</sup> These effects demonstrate broad potential applications in areas such as inducing apoptosis in cancer cells, promoting cell differentiation and proliferation, and neural modulation.<sup>4–6</sup> The development of safe and reliable hvNP generators is supported by innovations in power supplies, booster circuits, and chips. In many cases, the use of complex boosting circuits, chips, and appropriate power supplies is necessary, which often results in elevated costs and reduced stability.<sup>7,8</sup> As a result, achieving a balance between cost, stability, and safety in practical applications remains a significant challenge.

Lightning is a natural nanosecond pulse that does not require circuits, chips, or power supplies.<sup>9</sup> This reveals the possibility of generating hvNPs indirectly by tribocharging or contact charging. Various phenomena of triboelectricity, such as triboemission,<sup>10</sup> tribo-plasma,<sup>11</sup> and contact electrification,<sup>12</sup> have been discovered and investigated.<sup>13,14</sup> Triboelectric devices based on contact electrification offer advantages such as high voltage, low cost, and small size.<sup>15–18</sup> These devices show great promise for energy harvesting,<sup>19</sup> sensing,<sup>20–22</sup> environmental protection,<sup>23</sup> and biomedical applications.<sup>24–26</sup> However, triboelectric devices often have long discharge pulse widths and limited currents because triboelectric materials typically use dielectric materials with high impedance and low capacitance.<sup>27,28</sup> Therefore, to achieve hvNPs based on the contact electrification effect, it is necessary to overcome the limitations of high impedance, low capacitance, and low surface charge density in the contact electrification materials.<sup>29–31</sup>

Here, we have developed a Schottky nanodiode array-enabled triboelectric nanosecond pulse generator (st-NPG) with high voltage (10 kV), a duration in the nanosecond range (~60 ns), peak power (17 MW), single-pulse energy (0.6 J), and stability (7 days of operation), which eliminates the need for boosting circuits, chips, and external electrical power sources. This st-NPG is based on a highly ordered wafer-scale TiO<sub>2</sub> nanotube (TNT) array and Ti, which form Schottky barriers to facilitate the effective separation of positive and negative charges generated by contact electrification and enhance the accumulation of charges on the surface of TNTs and Ti. The design of the semiconductor TNTs and Ti achieves compatibility with low impedance, high capacitance, and high surface charge. Given the stability and high intensity of the generated nanosecond pulses, we have demonstrated their potential for medical applications. The hvNPs produced by the st-NPG achieved immunogenic death of tumor cells and pulsed ablation for tumor treatment via minimally invasive interventional surgery in both mouse subcutaneous tumors and rabbit liver tumors. This advancement provides a new pathway for reducing the cost (\$14.91, <1/1,000 of commercial cost) and complexity of high-voltage pulse generators while prolonging their stability and lifespan.

## RESULTS AND DISCUSSION

### High-performance NPG

The st-NPG consists of a stator, rotor, and spacer layer, as shown in [Figures 1A and 1B](#). The stator is primarily composed of a substantial area of highly ordered TNTs, which were formed by anod-

izing on the surface of a Ti electrode ([Figures 1C and S1–S3](#)). The rotor contains friction layers of polytetrafluoroethylene (PTFE) and nylon with opposite charge polarities, and the spacer layer's paper ridges are in contact with the friction layers to replenish the charge. When PTFE rubs against the paper, a negative charge is generated on the PTFE surface, and a positive charge is generated on the TNT surface. The presence of Ti/TNT results in the upward bending of the energy bands of TNTs, forming Schottky nanodiode arrays ([Figure S4](#)). The resulting Schottky barrier impedes the diffusion of positive charge to the Ti electrode, resulting in a significant accumulation of positive charge on the TNT surface ([Figure 1D](#)). Conversely, when nylon makes contact with the paper, the built-in Schottky electric field facilitates the flow of electrons from TNTs to the Ti electrode. Consequently, the electric potential distribution on the TNT surface is oriented opposite to that of the Ti surface. As the accumulated charge increases, the air in the gap between the TNT and the metallic Ti is broken down, creating a transient conducting channel. This results in the generation of high-voltage pulses with pulse widths of only nanoseconds in an external circuit ([Figure 1E](#)). The hvNPs generated by the st-NPG are sufficient to light up 50 commercial lamps rated up to 36 W ([Figure 1F](#); [Video S1](#)).

A study was conducted to investigate the voltage and energy variations of the st-NPG under different load resistances ([Figures 1G and S5–S9](#)). The results demonstrated that the output voltage can reach up to 10 kV, with the maximum peak power reaching up to 0.6 J. The peak powers of the high-voltage pulsed power supplies with load resistances in the range of 1–50 Ω were all greater than 1 MW, and the energies were all greater than 0.03 J. The peak voltage of the high-voltage pulsed power supply, 5.8 kV, was observed with a load resistance of 2 Ω, which corresponded to a peak power of 17 MW. The peak power of the high-voltage pulsed power supply was compared with output variations at different frequencies. It was found that the output stabilizes at approximately 8.5 kV when the frequency is greater than 2 Hz, providing a basis for the practical application of the st-NPG ([Figure 1H](#)). Currently, the maximum output frequency is 50 Hz due to restrictions in mechanical rotational energy. Future improvements, such as optimizing the triboelectric materials, structural designs, and rotational speeds, could help increase pulse frequencies to better meet clinical demands. In addition, the long-term stability of the high-voltage pulsed power supply is a crucial parameter. The high-voltage pulse power supply maintains the distance between the rotor and stator, significantly reducing the friction loss between them. It is capable of continuous and stable operation for over a week without any wear observed on the TNT ([Figures 1I and S10–S12](#)).

### Nanosecond electroporation promotes immunogenic death of tumor cells

The potential of hvNPs for clinical tumor ablation prompted us to investigate the st-NPG's ability to kill tumor cells.<sup>32–35</sup> The efficacy of hvNPs in killing cells was evaluated through an *in vitro* experiment. As illustrated in [Figure 2A](#), after treating the tumor cells with the st-NPG, evaluations were conducted on cell morphology, cytoskeleton, viability, and intracellular conditions. The results demonstrated a dose-dependent increase in tumor cell death rates, with late-stage apoptosis reaching

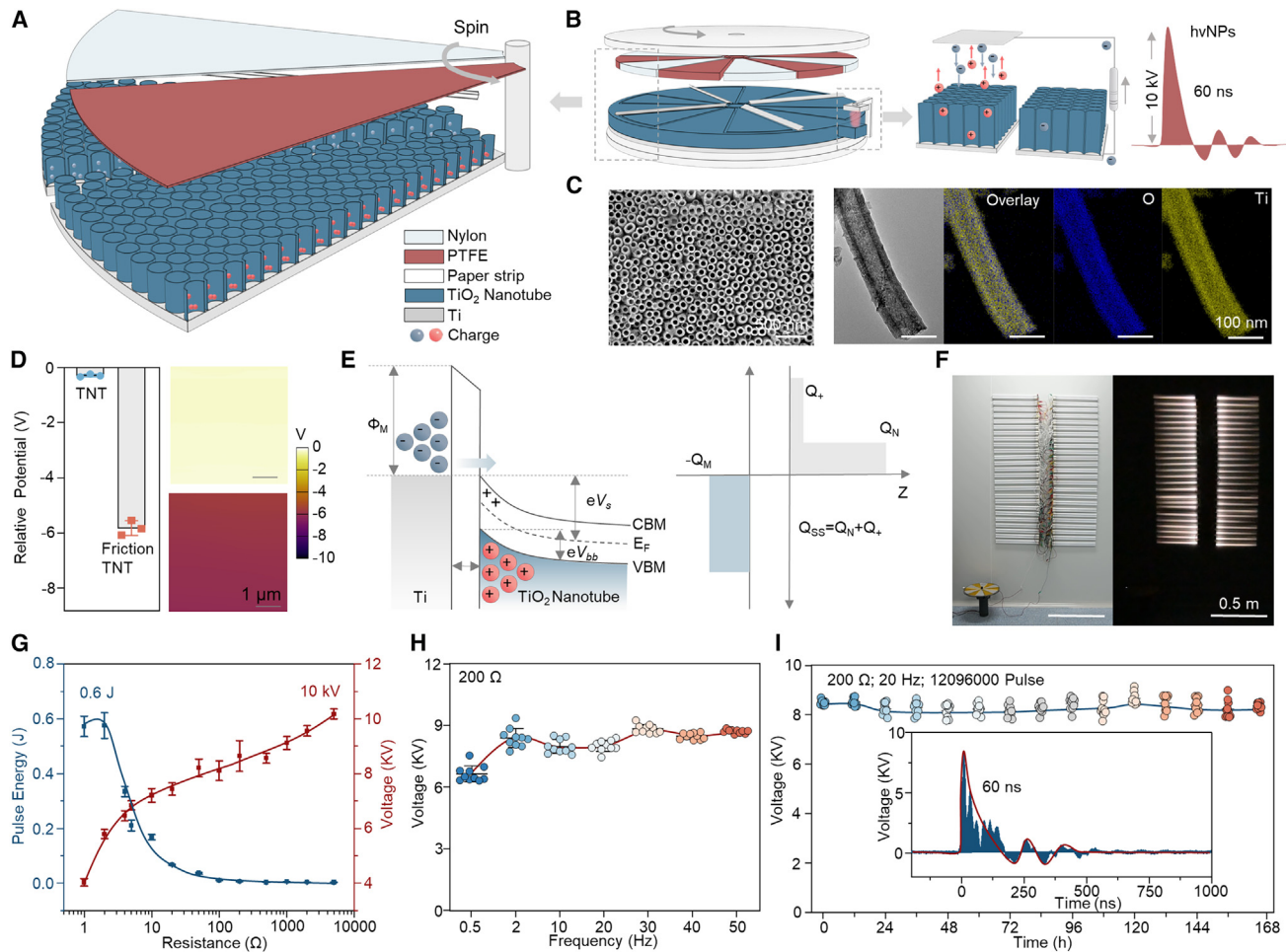


**Figure 1. Structural design and performance of the st-NPG**

- (A) Schematic diagram of the section of st-NPG. The st-NPG is composed of a rotor (friction layer nylon, PTFE), a stator (Ti/TNT), and a spacer (paper strip).  
 (B) A schematic diagram of the complete device accompanied by some enlargements.  
 (C) From left to right, the images are scanning electron microscope (SEM), transmission electron microscope (TEM), and energy-dispersive spectroscopy (EDS) of highly ordered titanium dioxide nanotubes.  
 (D) Kelvin probe force microscopy was employed to ascertain the surface potential distribution of TNT in both its as-received and friction-treated states.  
 (E) Energy band and charge balance diagrams.  
 (F) Photographs of 50 commercial 36 W lamps powered by st-NPG.  
 (G) High-voltage pulse source at varying resistive load voltages and pulse energies ( $n = 10$ ).  
 (H) Output voltage fluctuations at different frequencies under a  $200 \Omega$  resistive load, with a stable output at 2 Hz and above.  
 (I) The  $200 \Omega$  load resistor st-NPG maintains operational stability with a consistent output voltage.

$86.63\% \pm 2.4\%$  after 2 min of pulse exposure (Figure S13B). Cell Counting Kit-8 (CCK-8) assays revealed a significant decline in cell viability, with a reduction to  $10.9\% \pm 1.6\%$  after 1 min and  $1.9\% \pm 1.4\%$  after 2 min (Figure S13C). Moreover, pronounced killing effects were observed in both B16F10 and CT26 cells (Figure S13D). Propidium iodide (PI) staining was used to visualize the cell membrane perforation processes. Using gold-plated acupuncture needles as electrodes (Figure S14), the direct electrical stimulation of 4T1 cells with the st-NPG resulted in the rapid entry of PI from both ends of the cell, producing membrane blebbing and significant cell deformation over time. (Figure 2B; Video S2). Upon rectifying the electric pulses, electroporation first occurs on the cell membrane near the anode (Figure S15; Video

S3). As the electrode spacing increases, the ablation area also expands (Figure S16). Following the application of nanosecond pulses, a rapid increase in fluorescence intensity was observed in both 4T1 and bone marrow-derived macrophages (BMDMs) in the medium without calcium ions. This indicated a rapid increase in intracellular  $\text{Ca}^{2+}$ , as the electrical pulse triggered the release of  $\text{Ca}^{2+}$  from the endoplasmic reticulum. The intensity was maintained for more than 10 min in 4T1 tumor cells (Figure S17; Video S4). What is particularly noteworthy is that, for BMDMs, intracellular fluorescence gradually returned to normal levels, primarily due to the lower electrical sensitivity resulting from the smaller size of the cells and nuclei compared to 4T1 cells<sup>36</sup> (Video S5).

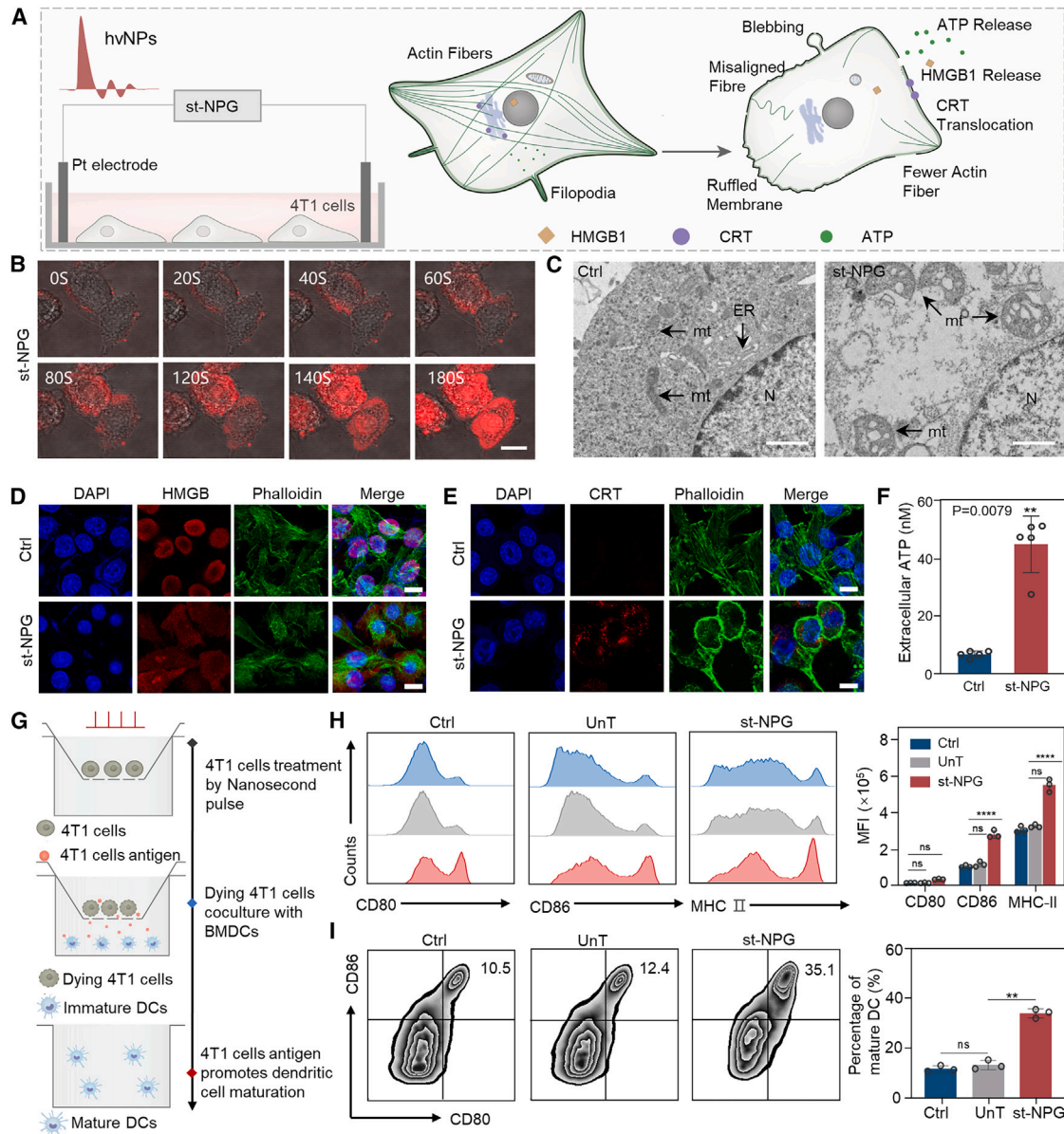


**Figure 2. Nanosecond pulses promote tumor immunogenic death and activate dendritic cells**

(A) Schematic representation of 4T1 cells stimulated by hvNPs and hvNP-induced actin disruption and immunogenic cell death.

(B) hvNP-induced cell membrane perforation, with PI dye entering the cell.

(C) Swelling of mitochondria was immediately observed in 4T1 tumor cells in mice after hvNP exposure with 3-mm bi-electrodes. mt, mitochondria; ER, endoplasmic reticulum. Scale bar: 1  $\mu$ m.

(D) Fluorescence microscopy images of HMGB1 (red fluorescence). Scale bar: 10  $\mu$ m.

(E) Fluorescence microscopy images of calreticulin (red fluorescence) expressed by 4T1 cells under electrical stimulation. Scale bar: 10  $\mu$ m.

(F) ATP content released by 4T1 cells after electrical stimulation ( $n = 5$ ).

(G) Schematic diagram of experimental design for *in vitro* 4T1 cell and BMDC co-culture assay using transwell system.

(H) Representative FC histograms of the cell surface expression of co-stimulatory molecules (CD80, CD86, and MHC class II) on BMDCs at 24 h following treatments (left) and quantitative analysis the mean fluorescence intensity (MFI) of CD80, CD86, and MHC class II from FC results (right) ( $n = 3$ ).

(I) Representative flow cytometric plots of mature DCs (CD80<sup>+</sup>CD86<sup>+</sup>) following various treatments (left) and corresponding quantitative analysis results (right) ( $n = 3$ ). In (F), (H), and (I), data are presented as mean  $\pm$  SD, and statistical significance was determined by unpaired t test or the one-way ANOVA, \*\* $p < 0.01$ , \*\*\* $p < 0.001$ , \*\*\*\* $p < 0.0001$ .

After electroporation, the morphology of 4T1 cells was observed, revealing a rounded appearance indicative of cellular fragmentation. The contents of the cells leaked out, and the nucleus was apparent under a scanning electron microscope (SEM), accompanied by the disappearance of cell surface folds (Figure S18). Transmission electron microscope (TEM) revealed post-electroporation cellular changes, including chromatin aggregation, cytoplasmic condensation, vacuoles in the cytoplasm, and mitochondrial swelling and degeneration. Additionally, no filopodia-like protrusions were observed on the cell membrane (Figure 2C). Immunofluorescence staining showed disordered cytoskeletal structures (Figure S19), high-mobility group box-1 protein (HMGB1) leakage into the cytoplasm (Figure 2D), calreticulin (CRT) translocation to the cell membrane (Figure 2E), and adenosine triphosphate (ATP) secretion from cells (Figure 2F), indicating that cells underwent immunogenic death.<sup>37</sup> Co-culturing of immature dendritic cells with electroporated tumor cells revealed the upregulation of CD80, CD86, and major histocompatibility complex (MHC) class II surface markers (Figures 2G and 2H), with the percentage of CD80<sup>+</sup>CD86<sup>+</sup> dendritic cells increasing from 10.5% ± 0.97% to 35.1% ± 1.46%, indicating that the dead cells can activate dendritic cell maturation (Figure 2I).

### Nanosecond pulse stimulation induces tumor ablation and immunity activation

Following the determination of the tumor-killing effect of nanosecond pulses, an *in vivo* tumor treatment experiment was performed (Figure 3A). Finite element analysis was used to investigate the impact of varying distances between electrodes on local electric field strength within a tumor. It was observed that when a voltage of 10 kV was applied, the central electric field amplitude between the two electrodes reached 50 kV/cm, which is sufficient to meet the requirements for cell electroporation<sup>38</sup> (Figure S20). Local temperature elevation due to hvNP and microsecond pulse (MP) stimulation did not exceed 1°C, thus minimizing thermal damage (Figures 3B and S21). Meanwhile, nanosecond pulses are less likely to cause muscle tremors and twitching than MPs (Videos S6 and S7). In a mouse model bearing 4T1 tumors, those treated with nanosecond pulses exhibited significant tumor clearance (Figure 3C). The st-NPG group showed significant improvement in inhibiting primary tumor growth, with tumor growth notably slowed down. In this group, 4 out of 5 mice had complete tumor clearance, and at day 14, there was a significant difference in tumor volume compared to the sham group ( $p < 0.0001$ ) (Figures 3D and S22A–S22C). The spleen of the sham group was significantly enlarged, and its weight was 2.45 times that of the st-NPG group (Figures S22D and S22E). This pronounced therapeutic efficacy contributed to an extended survival duration, with 6 out of 8 mice surviving for 2 months, while in the sham group, all mice died within about 6 weeks (Figure 3E).

The subsequent objective was to ascertain whether the nanosecond pulses generated by the st-NPG could stimulate the immune system. Flow cytometry (FC) analysis on day 5 post-electroporation further quantified T cells in mouse tumors and lymph nodes (Figures S23 and S24). The data demonstrate a significant increase in the percentage of CD8<sup>+</sup> T cells within the tumors,

from 20.5% ± 0.7% to 26.2% ± 2.5%, and a notable rise in the percentage of CD4<sup>+</sup> T cells, from 32.8% ± 7.4% to 51.9% ± 8.4%, compared to the sham group (Figure 3F). Furthermore, as a principal effector cell of antitumor immunity, CD8<sup>+</sup> T cells in tumor-draining lymph nodes exhibited a 1.24-fold increase compared to the control group, indicating that electrical stimulation augmented T cell activation in the lymph node (Figure 3G). Hematoxylin and eosin (H&E) staining demonstrated near-complete tumor cell death following nanosecond electroporation. Immunohistochemistry confirmed tumor cell apoptosis and significant inhibition of tumor cell proliferation (Figure 4H). Additionally, Figures S25 and S26 indicated that hvNP electric stimulation had no significant impact on vital organs and blood routine, suggesting good biosafety.

### Nanosecond pulses inhibit distal tumor growth

To validate the immunogenic activation of nanosecond pulses, we evaluated their inhibitory effects on distant tumors (Figure 4A). Tumor growth curves under different treatment conditions are shown in Figure 4B, indicating that the st-NPG group markedly impeded the expansion of the primary tumor and exhibited a notable difference in the primary tumor's weight ratio ( $p < 0.0001$ ). Furthermore, the distant tumor exhibited a discernible degree of inhibition compared to the sham group (0.087 ± 0.11 g), with a mean weight of 0.035 ± 0.05 g ( $p = 0.0107$ ) (Figures 4C and 4D). Furthermore, the st-NPG group exhibited a reduction in lung metastases, which suggests a diminished prevalence of distal metastases (Figures 4E and S27). At the same time, a significant effect on the body weight of the mice was observed during treatment (Figure S28). Accordingly, the nanosecond electrical pulses generated by st-NPG can induce the immunogenic death of tumor cells, promote the maturation of dendritic cells, activate T cells in the tumor and draining lymph nodes, and inhibit the growth of distal tumors and lung metastasis during tumor ablation (Figure 4F).

### Nanosecond-pulse-mediated hepatic tumor ablation

To further evaluate its therapeutic effect on larger tumors, we established a rabbit VX2 subcutaneous transplant model and performed terminal deoxynucleotidyl transferase dUTP nick end labeling (TUNEL) and H&E staining 3 days after treatment, demonstrating effective tumor cell killing (Figure S29), with no significant damage to major organs (Figure S30). Subsequently, we established a rabbit liver VX2 *in situ* tumor model and used ultrasound-guided ablation needles for tumor ablation (Figures 5A and S31; Video S8). Computed tomography (CT) enhancement scans before ablation of rabbit liver tumors showed low-density nodules under the left lobe capsule, approximately 1.0–1.3 cm in diameter, with mild irregular enhancement around them (Figure S32). The st-NPG was used to apply 200 electrical pulses to the liver, each with a single-pulse energy of about 5.12 mJ and a half-peak width of about 60 ns (energy conversion efficiency is about 2.18%). The electromyographic signals generated by hvNP induction were detected in the heart without affecting its normal beating (Figure 5B). The detected applied voltage reached 10.2 kV (Figure 5C), and the peak power was 0.13 MW (Figure 5D).

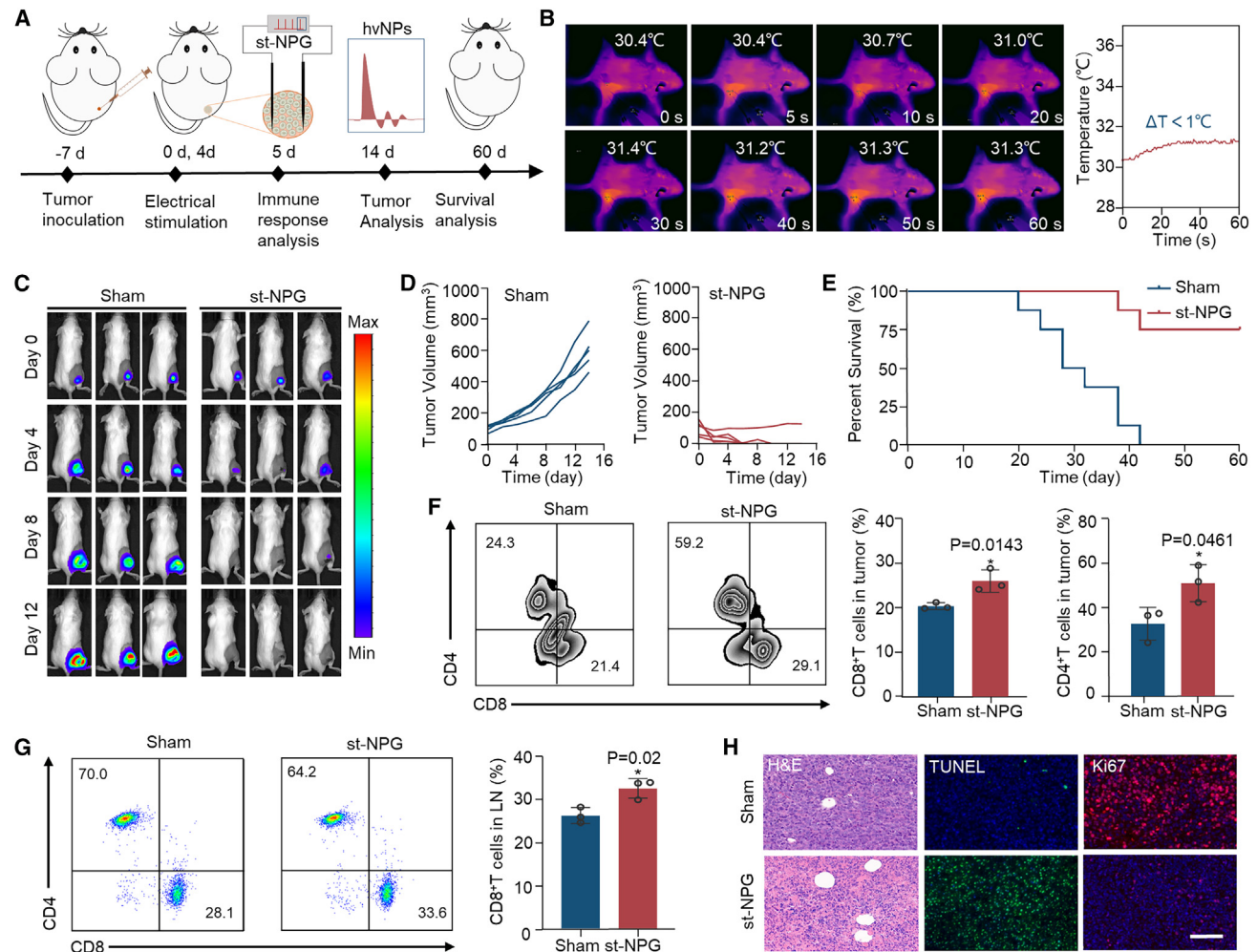


**Figure 3. Nanosecond pulses mediated subcutaneous 4T1 tumor therapy *in vivo***

(A) Schematic illustration of the *in vivo* treatment process.

(B) Local temperature changes of mice during the ablation by infrared camera.

(C) Representative images of tumor burden obtained by bioluminescent imaging.

(D) Individual tumor growth curves for mice after different treatments.

(E) Survival curves for mice of the different groups.

(F) The proportion of CD4<sup>+</sup> and CD8<sup>+</sup> T cells in tumor tissues was analyzed by FC ( $n = 3$ ).

(G) The proportion of CD4<sup>+</sup> and CD8<sup>+</sup> T cells in lymph node was analyzed by FC ( $n = 3$ ).

(H) Representative H&E, TUNEL, and Ki67 staining of tumor ablation areas. Scale bar: 100  $\mu$ m.

In (F) and (G), data are presented as mean  $\pm$  SD, and statistical significance was determined by unpaired t test, \* $p < 0.05$ .

The liver tumor presents as a thick, circular area of high enhancement in the arterial phase (Figure 5E, left). After ablation, the tumor was completely necrotic, with no contrast agent perfusion observed in the arterial stage. Third-phase angiography showed that the necrotic area was significantly larger than that of the primary tumor (Figure 5E, right). A CT scan immediately after ablation showed that the ablation area completely covered the tumor, and the tumor did not enhance, indicating that the ablation was complete (Figure 5F). H&E staining immediately after surgery showed significant tumor necrosis (Figure S33). Compared with the sham group, the tumor diameter increased to 155.5% after 1 week, while the tumor diameter decreased

to 80.6% in the st-NPG group, demonstrating significant inhibition of tumor growth (Figure 5G). Intraoperative monitoring showed no significant differences in heart rate or ejection fraction between the treated and sham groups (Figure S34).

### Conclusions and outlook

In this study, we present a high-voltage NPG that does not require an external electrical power supply, chip, and complex boosting circuit based on the triboelectric effect. The highly ordered, wafer-scale semiconducting TNT arrays prepared on titanium electrodes were used as contact-electrification materials, enabling charge storage and rapid separation through Schottky

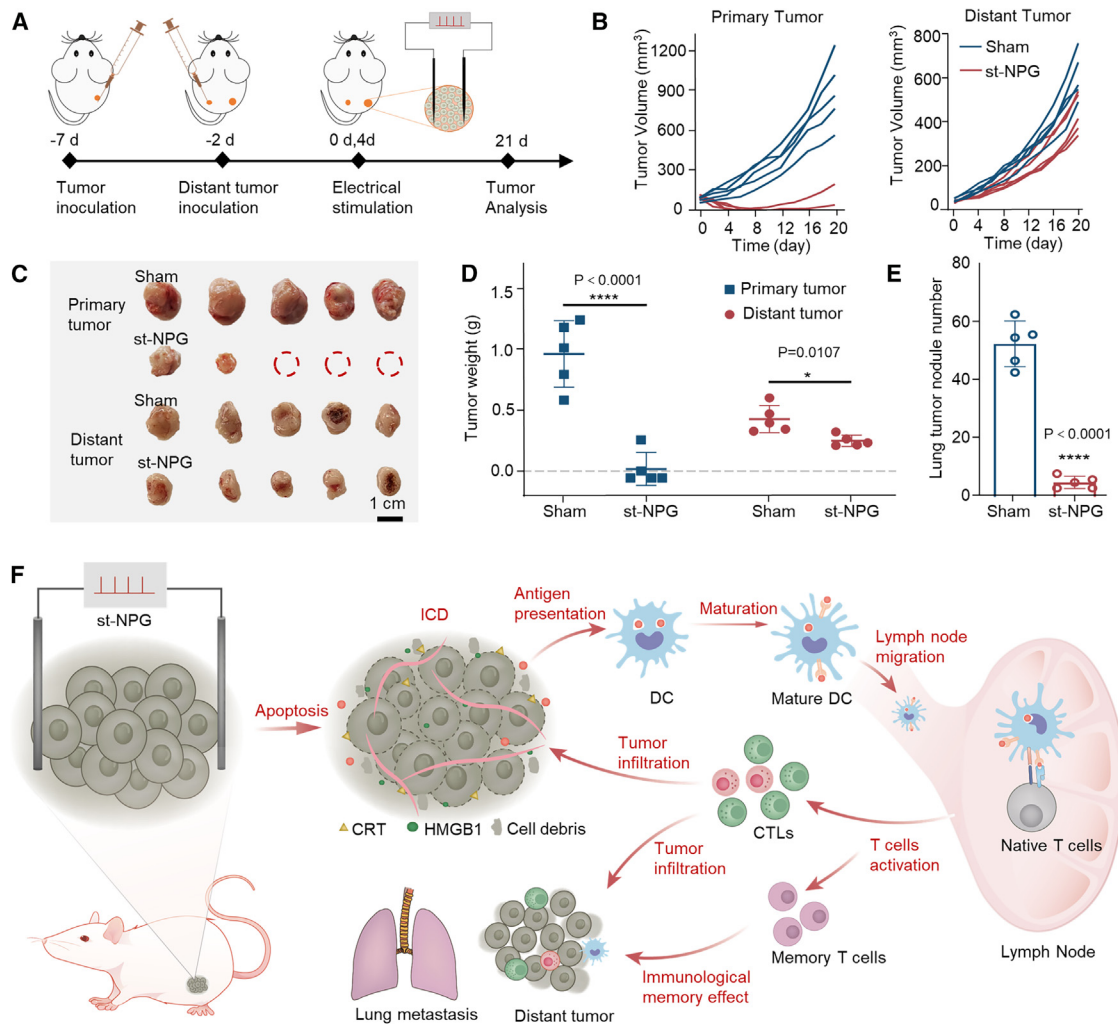


**Figure 4. Nanosecond pulse ablation inhibited distal tumor growth**

(A) Schematic illustration of the *in vivo* treatment process.

(B) Growth curves of tumor *in situ* and distant tumor in mice after different treatments.

(C) Representation images of primary tumor and distant tumor after treatment.

(D) Weight of primary and distant tumors (n = 5).

(E) Number of macroscopic tumor nodules on lung surface (n = 5).

(F) Schematic illustration of st-NPG induces immunogenic death of tumor cells, promotes activation of T lymphocytes after dendritic cells mature, and inhibits distal tumor growth and lung metastasis.

In (D) and (E), data are presented as mean  $\pm$  SD, and statistical significance was determined by unpaired t test, \* $p < 0.05$ , \*\*\*\* $p < 0.0001$ .

contacts. This power-source-free generator can generate pulses of up to 10 kV with a width of 60 ns, a peak power of 17 MW, and an energy of 0.6 J. Furthermore, the generator demonstrated sustained high-voltage output over a 7-day period. *In vivo* studies using the high-voltage NPG in a mouse subcutaneous transplantation tumor model revealed its efficacy in tumor ablation, elimination of primary tumors, and inhibition of distant tumor growth. Promising results were also observed in a rabbit *in situ* hepatocellular carcinoma model, which is characterized by high vascularity. Given that nanosecond pulses represent a non-thermal ablation technique with well-defined ablation boundaries and minimal damage to surrounding healthy tissues,

they are particularly well suited for the ablation of tumors in close proximity to nerves and blood vessels. At the same time, the structures, such as blood vessels and nerves, within the ablation zone are preserved, facilitating postoperative tissue repair. Moreover, the potential for muscle twitching and cardiac side effects associated with MP ablation can also be mitigated. The minimalist design of the st-NPG offers significant advantages in terms of both reliability and cost effectiveness. With a material cost of only around \$15, it is a fraction of the price of commercial NPGs, which typically cost tens of thousands of dollars. This cost efficiency, along with its excellent output performance and reliability, makes the st-NPG a highly promising technology.

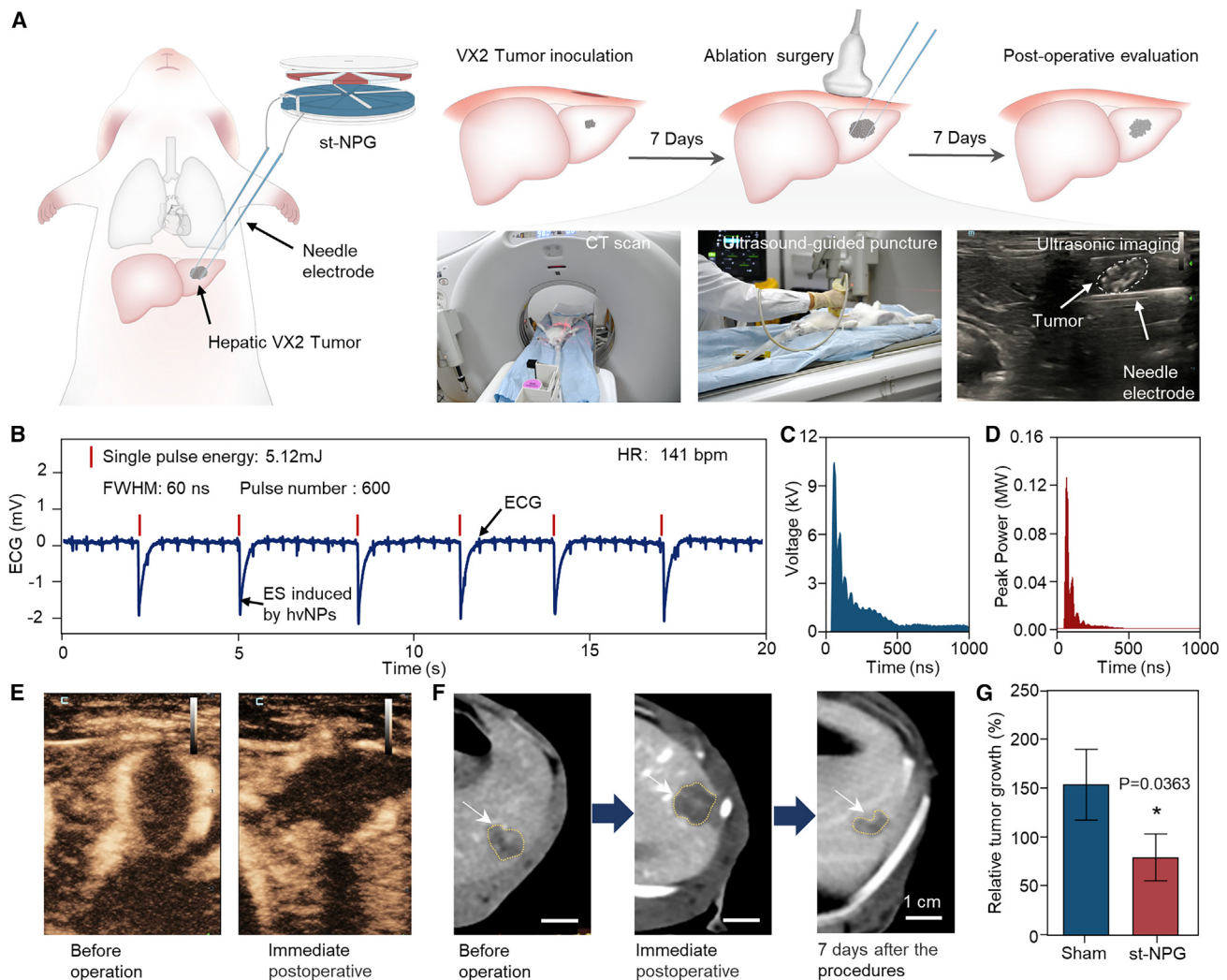


**Figure 5. Evaluation of the effect of st-NPG *in situ* liver cancer ablation in rabbits**

(A) Schematic diagram of st-NPG interventional ablation.  
 (B) Rabbit electrocardiograph (ECG) signals monitored during ablation surgery.  
 (C) Waveform of voltage pulse applied during ablation.  
 (D) Peak power of electrical pulse during ablation.  
 (E) Contrast-enhanced ultrasound images before and after ablation.  
 (F) Computed tomography images of tumor sites before and after ablation.  
 (G) Relative growth rates of tumors in the sham operation group and the treatment group before treatment ( $n = 3$ ).  
 In (G), data are presented as mean  $\pm$  SD, and statistical significance was determined by unpaired t test,  $*p < 0.05$ .

Its novel design and use of low-cost materials position it for widespread adoption, particularly in resource-constrained regions where affordability is crucial.

Looking ahead, future research can focus on several key directions. First, efforts should be made to optimize the device for higher energy density, higher energy conversion efficiency, and increased parameter adjustability.<sup>39,40</sup> By improving material selection, optimizing charge storage and separation mechanisms, and enhancing power supply efficiency, the energy output and peak power of the NPG could be further increased. Pulse frequency can be adjusted within a certain range by

changing the rotational speed of the device, while pulse voltage and width can be modulated by altering electrode spacing, incorporating modulation circuits, or adjusting the breakdown atmosphere.<sup>41,42</sup> This would better meet the high-energy and variable parameter demands in both biomedical treatments and industrial applications. Second, expanding its biomedical applications is a key avenue for future work. Research can explore the potential of nanosecond pulses in treating a wider range of diseases, such as tissue repair and immune modulation. By adjusting pulse parameters, therapeutic outcomes can be optimized, improving clinical applicability and safety.

Additionally, extending the application of nanosecond pulses in environmental and industrial fields, such as in water treatment, gas purification, and material surface modification, could offer new solutions for environmental protection and industrial processes. Another important research direction is cost reduction and scalability, particularly for regions with limited resources. Optimizing the design and manufacturing processes of the device will be crucial to enabling the widespread adoption of this technology. Finally, interdisciplinary collaboration will play a vital role in advancing the development of nanosecond pulse technology. By integrating the latest advancements in physics, electronic engineering, materials science, and medicine, we can foster technological innovations and expand the applications of this technology.

In summary, the st-NPG has vast application potential. Continued optimization and interdisciplinary collaboration in the future will promote its widespread use in biomedical, environmental protection, and industrial production, offering new technological solutions for these fields.

## METHODS

### Preparation of TNTs

A 1-mm-thick titanium electrode was chemically polished for 3 min in a solution of 40% nitric acid, 10% hydrofluoric acid, and 50% deionized water. The electrode was then subsequently sonicated in acetone, alcohol, and deionized water for 30 min. After drying, the titanium electrode was cleaned in a plasma cleaner for 3 min. Next, a positive photoresist (S1813) was spin coated onto the electrode using a spin coater (1,000 rpm for 10 s, followed by 7,000 rpm for 30 s) and dried at 80°C for 10 min. The sample underwent anodic oxidation at 60 V (using a high-voltage power supply, MCH-K1505D) in a dual-electrode configuration, with a carbon electrode placed 1 cm away from the titanium electrode. The electrolyte consisted of 90% ethylene glycol, 5% deionized water, 5% methanol, and 0.55% ammonium fluoride by mass. Anodization lasted for 55 min. Afterward, the samples were immersed sequentially in acetone, alcohol, and deionized water for 1 h and then dried in a 60°C oven. Finally, the sample was annealed in air using a tube furnace at a heating rate of 5°C/min, reaching a temperature of 450°C, with a holding time of 3 h, followed by natural cooling in the furnace.

### Characterization of TNT

Microscopic morphological observations of the TNT were performed using a field-emission SEM (NOVA450, Czech Republic) at an accelerating voltage of 10 kV. Crystal and elementary compositions were analyzed by an X-ray diffractometer (PANalytical X'Pert) with Cu K $\alpha$  radiation. Raman spectra were recorded using an Ar laser operating at a wavelength of 532 nm (LabRAM HR Evolution, Horiba) at room temperature. Ultraviolet photoelectron spectroscopy (UPS) was performed on the Thermo Scientific ESCALab 250Xi. The gas discharge lamp was used for UPS, with helium gas admitted and the He I emission line at 21.22 eV employed. The helium pressure in the analysis chamber during analysis is about  $3 \times 10^{-8}$  mbar. X-ray photoelectron spectroscopy (XPS) was performed on the Thermo Scientific ESCALab

250Xi using 200 W monochromatic Al K $\alpha$  ( $h\nu = 1,486.6$  eV) radiation. The 500  $\mu\text{m}$  X-ray spot was used for selected area XPS analysis. The base pressure in the analysis chamber was about  $3 \times 10^{-9}$  mbar. Typically, the hydrocarbon C1s line at 284.8 eV from adventitious carbon was used for energy referencing.

### Fabrication of nanosecond pulse high-voltage generator

The nanosecond pulse power source comprises a stator and a rotor. An acrylic disk (30 cm diameter, 5 mm thickness) was cut using a laser cutting machine. Custom titanium metal sector-shaped electrodes (1 mm thick) were anodized *in situ* to generate TNTs on the titanium surface. Twelve sector-shaped Ti/TNT electrodes were uniformly distributed on the acrylic disk, with a 3-mm gap between each sector. The PTFE film and nylon film (100  $\mu\text{m}$  thick) were cut into 6 sectors each and distributed uniformly on the rotor. A rectangular paper strip (130 mm long, 10 mm wide) was cut from a tissue and folded at its center. The tissue was stacked and adhered in the gap between a pair of Ti/TNT sector electrodes, forming a small paper spine between the two electrodes. By adjusting the distance between the stator and the rotor, the paper spine makes contact with the PTFE and nylon films while maintaining a fixed distance between the rotor and the stator. The NPG was driven by a variable-speed rotating electrode. The open circuit voltage was measured using an oscilloscope (Teledyne LeCroy WAVERUNNER 9104) and a high-voltage probe (Tektronix p6015A).

### Animal and cell lines

4T1 cells were cultured in Dulbecco's modified Eagle's medium (DMEM; Gibco, USA) supplemented with 10% fetal bovine serum (FBS; Gibco, USA) and 1% penicillin/streptomycin in a humidified incubator with a 5% CO<sub>2</sub> atmosphere at 37°C. B16F10 and CT26 cells were cultured in RPMI 1640 medium with 10% FBS and 1% penicillin/streptomycin. After reaching 80% confluence, the cells were passaged or used for experiments.

BALB/c mice were purchased from Beijing Vital River Laboratory Animal Technology. New Zealand white rabbits were purchased from Tianjin Yuda Laboratory Animal Breeding. All protocols were approved by the Institutional Animal Care and Use Committee.

### Cell-membrane damage evaluated by cell uptake of PI

A single layer of 4T1 cells was seeded on a confocal dish and incubated overnight. hvNP-induced transient cell membrane damage was evaluated through diffusion-based cell uptake of PI (Solarbio) and the subsequent fluorescence signals. Cells were cultured in DMEM with 10% FBS containing 2  $\mu\text{g}/\text{mL}$  PI. Two gold-plated needle electrodes (0.25 mm diameter, 13 mm length) connected to the st-NPG were placed in parallel, 3 mm apart, perpendicular to the bottom of the confocal dish. The cells were stimulated with continuous electrical pulses at a frequency of 30 Hz using the st-NPG. Fluorescence live-cell imaging was performed using a laser scanning confocal microscope (Leica SP8).

### Cell viability assay

The effects of hvNPs on the cell viability of 4T1, B16F10, and CT26 cells were analyzed using the CCK-8 assay. Cells at the

logarithmic growth stage were digested with 0.25% trypsin, centrifuged at 1,000 rpm, and re-suspended in a 5% mannitol:DMEM with 10% FBS (1:1) solution. The cell suspension was placed in an electroporation cuvette with an electrode gap of 1 mm and treated with hvNPs. After treatment, the cell suspension was removed from the Petri dish, re-suspended in fresh medium, and inoculated in 96-well plates for 6 h. After 6 h, the cells were washed twice with DMEM. A mixture of 110  $\mu$ L containing medium and CCK-8 reagent was added in the dark. The cells were then incubated for 1–2 h. The absorbance of each experimental sample was measured at 450 nm using a microplate reader (Varioskan LUX, Thermo Scientific). All data were normalized against the control (untreated hvNPs) groups to assess cell viability.

#### **Annexin V-FITC/PI staining assay**

Cell apoptosis was assessed by an Annexin V-FITC Apoptosis Detection Kit (Multisciences Biotech., China). After hvNP treatment, the cell suspension was removed from the cuvette and stained with annexin V-fluorescein isothiocyanate (FITC) and PI according to the manufacturer's instructions. Apoptosis was then analyzed by flow cytometry (Beckman Coulter).

#### **TEM**

We observed the morphological changes of 4T1 cells treated with pulsed electric fields using TEM. 4T1 cells treated with pulsed electric fields were immediately fixed overnight with 3% glutaraldehyde and then washed with PBS. The cell sample was immersed in PBS containing 1% osmic acid for 2 h and then washed three times with PBS. The sample was dehydrated with a series of different concentrations of ethanol (50%, 70%, 80%, 90%, and 100%) and twice with 100% acetone. After embedding with an embedding agent, ultra-thin sections were obtained using an ultra-thin slicing machine. After staining the sample with uranium acetate (5%) and lead citrate (1%), we observed the sample using TEM (Hitachi-7700).

#### ***In vitro* assessing the effect of hvNP-triggered calcium release**

The cultural conditions for 4T1 cells and BMDMs were described above, and the cells were incubated with 1  $\times$  Fluo-4 Direct calcium reagent loading solution (Thermo Scientific, F10471) at 37°C for 1 h. The fluorescence changes before and after stimulation with 3-s electrical pulses were recorded by a confocal laser scanning microscope (CLSM) (Leica SP8). We performed point-in-time imaging and demonstrated the concentration changes of calcium in cell with elapsed time.

#### **Determination of CRT, HMGB1, and ATP from hvNP-treated cells**

After treatment with hvNPs, 4T1 cells were subjected to confocal imaging. Following electrical stimulation of 4T1 cells, the cells were immediately incubated with primary antibody against CRT (1:200, Cell Signaling Technology, Danvers, MA, USA) for 30 min, followed by staining with Alexa Fluor 647-labeled goat anti-rabbit secondary antibody (1:500, Beyotime Biotechnology) and counterstained with DAPI. Then, the exposure of CRT was observed by CLSM. After electrical stimulation of 4T1 cells, the cells were fixed with 4% paraformaldehyde and permeabilized

with cold methanol. They were then incubated with primary anti-HMGB1 antibodies (1:200, Abcam) overnight, followed by incubation with an Alexa Fluor 647-labeled goat anti-rabbit secondary antibody. The release of HMGB1 was detected through CLSM. Extracellular ATP concentrations were quantified by the ATP Assay Kit (Beyotime Biotechnology).

#### ***In vitro* BMDc culture and activation**

Bone marrow-derived dendritic cells (BMDcs) were obtained from the femur of BALB/c mice, which were euthanized and isolated. The femurs were washed with cold PBS and transferred to culture medium, and the ends of the femurs were cut open to rinse out the bone marrow cells with PBS. The cells were passed through a 70  $\mu$ M filtration mesh. Cells were harvested and lysed using red blood cell lysis buffer for 5 min. After centrifugation at 350g for 10 min, the obtained bone marrow cells were suspended in RPMI 1640 medium containing 10% FBS, granulocyte macrophage colony-stimulating factor (GM-CSF; 10 ng/mL), and interleukin (IL)-4 (10 ng/mL) and cultured for 7 days to obtain immature BMDcs. Immature BMDcs ( $5 \times 10^4$  cells/well) were seeded into 24-well plates and divided into three groups: the control (Ctrl) group, which contains only BMDcs; the UnT group, where untreated 4T1 cells ( $1 \times 10^4$  cells) were added; and the st-NPG group, where an equal number of 4T1 cells were placed in an electroporation cuvette and treated with the st-NPG for 2 min before co-culturing with the dendritic cells. After co-incubation for 24 h, BMDcs were stained with antibodies (anti-CD11c-APC, anti-MHC class II-PC7, CD80-FITC, and anti-CD86-PE) and analyzed by flow cytometry.

#### **Finite element analysis of the electrode system based on COMSOL software**

The finite element calculation software COMSOL Multiphysics was used to simulate and estimate the behavior of the electrode system in a solution environment. The model size refers to the actual dimensions of the electrodes and the water body. The electric field distribution and related electrical characteristics between the electrodes were calculated after applying the potential difference. The electrode material was gold, and the liquid environment was a solution with relative permittivity of 305. The electrode radius was 0.25 mm, the spacing between electrodes was 10 mm, and the water body radius was 10 mm. A potential difference of 10 kV was applied between the two electrodes.

#### **Collection and culture of primary BMDMs**

The procedure of bone marrow cell extraction was the same as that of BMDcs. Bone marrow cells were obtained after centrifugation and re-suspended with  $\alpha$ -MEM medium containing 50 ng/mL M-CSF (PeproTech). After 5–7 days, we used a cell scraper to collect the mature BMDMs.

#### ***In vivo* evaluation of anticancer efficacy in 4T1 model**

On day 0, 6- to 8-week-old male BLAB/c mice were inoculated subcutaneously with  $5 \times 10^5$  4T1-Luc1 cells on their right thigh. Ablation surgery was performed when the tumor reached 100 mm<sup>3</sup>. To ensure tumor ablation, two gold-plated acupuncture needles were inserted parallel into the tumor site, with a 3 mm interval between them, and each location was ablated for 3 min before switching to a new ablation site. The size of

the tumors and percentage of survival were measured at regular intervals, and the experimental endpoint was defined as either death or a tumor size greater than 1,500 mm<sup>3</sup>. Tumor volumes were calculated by

$$V = \frac{L \times W^2}{2},$$

where L is the longest diameter of the tumor and W is the shortest diameter of the tumor (mm).

### Evaluation of the effect on tumor inhibition by immunohistochemical section

After the completion of electroporation, mice were taken from each group for immunofluorescence sectioning and then imaging. Proliferating cell nuclear antigen-Ki67 was used to determine the nucleus proliferation of tumor tissue. Terminal deoxynucleotidyl TUNEL staining was used to detect the DNA breaks in the last phase of apoptosis.

### In vivo biocompatibility evaluation

After treatments, routine blood examinations were performed. The animals were sacrificed, and the primary organs were harvested, fixed in 4% formalin overnight, and then embedded in paraffin for H&E staining.

### Evaluation of cellular recruitment and activation

On day 5 post-electroporation, three mice from the sham and st-NPG group were euthanized. The tumor and inguinal lymph nodes were extracted, thoroughly cleaned, and cut into fragments. Then, the tissue was digested at 37°C in PBS containing 0.2% collagenase D and 100 U/mL recombinant DNA enzyme I (Roche Diagnostics) for 2 h. The digested tissue was prepared into a single-cell suspension through a 40-μm cell filter and further stained with a combination of the following antibodies: PC-7-CD45, PC5.5-CD3, APC-CD4, and FITC-CD8. Subsequently, the cells were analyzed using flow cytometry.

### Establishment of rabbit liver VX2 tumor model

Six female New Zealand white rabbits (1.5–2.0 kg) were purchased from Tianjin Yuda Laboratory Animal Breeding. All rabbits used the VX2 tumor cell line to establish the liver orthotopic model. All experimental procedures were conducted in strict accordance with institutional and national guidelines for the care and use of laboratory animals. The study protocol was approved by the Medical Ethics Committee of Tianjin Medical University General Hospital (ethical approval no. IRB2022-DW-76).

The VX2 tumor was minced to create a tissue suspension, and approximately 1 mL of the suspension was injected into the thigh muscle of rabbits. Two weeks later, the tumor tissue was carefully excised under aseptic conditions and trimmed to 1–2 mm<sup>3</sup>. It was then stored in an ice bath. Following general anesthesia, the limbs of the rabbit were immobilized, and the skin was prepared. A 3-cm longitudinal incision was then made along the midline of the abdomen just below the xiphoid process. The liver was clamped with toothless forceps and pulled out of the abdominal cavity. A "flask"-shaped sinus was created in the thicker part of the left

central lobe using ophthalmic forceps to form a small opening (3–5 mm) with a wide base (5–8 mm). Two to three pieces of minced tumor tissue were implanted into the sinus, which was filled with gelatin sponge fragments. After confirming no obvious bleeding, the liver was returned to the abdominal cavity, and the abdomen was closed layer by layer. The incision was cleaned with normal saline. Penicillin was administered intramuscularly for 3 days postoperatively to prevent infection. One week following the transplantation of the tumor strains, the experiment began.

### Nanosecond pulse ablation in the treatment of rabbit liver tumors *in situ*

The rabbits were divided into two groups: one group underwent sham surgery and the other received electrical stimulation. Prior to the surgical procedure, the rabbits were fasted for 12 h and then anesthetized by inhalation of isoflurane (3%–4% for induction and 1%–2% for maintenance). Once adequately anesthetized, the rabbit was fixed on the CT examination bed, and contrast-enhanced CT scanning was performed using the contrast agent iodixanol at a rate of 0.8 mL/s and a total volume of 3 mL to observe the tumor size, location, and enhancement method.

Concurrently, a bolus injection of 0.5 mL of the contrast agent SonoVue (Bracco, Italy) was administered into the marginal ear vein of the rabbit. Grayscale ultrasound scanning was then employed to observe and record the contrast enhancement in the rabbit's liver tumor prior to ablation (ultrasonic probe L18-5, Mindray M9, China). Two ablation needles were inserted into the liver in parallel and positioned at the edge of the tumor under the guidance of contrast-enhanced ultrasound. The two ablation electrodes were exposed to a depth of 1 cm, with the distance between the ablation needles being approximately 1 cm (ablation voltage: 10 kV, pulse width: 600 pulses). The treatment was initiated, and changes in the rabbit's heart rate and respiratory patterns were monitored. Subsequently, contrast-enhanced ultrasound and CT scans were conducted under identical conditions to assess the extent of tumor ablation. A CT scan was conducted 1 week after surgery to assess the condition of the tumor following ablation.

### Calculation of the peak power density and pulse energy

Peak power was employed to evaluate the generator output performance. The following equation can derive the output power:

$$\text{peak power} = U^2/R.$$

E is the pulse energy,

$$E = \int U^2 / R dt,$$

where R is the load resistance and U is the voltage at both ends of the load resistance.

### Calculation of energy conversion efficiency

To quantify the performance of the st-PNG, we calculated the average conversion efficiency of mechanical energy into

electrical energy. First, we computed the rotational kinetic energy of the rotor:

$$T_{\text{rot}} = \frac{1}{4}mr^2\omega^2.$$

$T_{\text{rot}}$  represents the rotational kinetic energy,  $m$  the mass of the disk,  $r$  the radius of the disk, and  $\omega$  the angular velocity.

The  $m = 0.437$  kg,  $r = 0.16$  m, and  $\omega = 18.3$  rad/s, resulting in a rotational kinetic energy  $T_{\text{rot}} = 0.936$  J. During the animal experiments, when the angular velocity decayed from 8.05 to 0 rad, a total of 4 pulses were generated, each with an energy of 5.12 mJ.

$$\eta = \frac{E_{\text{out}}}{T_{\text{rot}}}$$

### Calculation and statistical analysis

Data are presented as the mean  $\pm$  standard deviation (SD). Statistical analyses were performed using the Origin software program and Prism 8.0 software (GraphPad Software), applying one-way ANOVA and an unpaired Student's  $t$  test. The  $p$  values for all experiments were considered significant at  $*p < 0.05$ ,  $**p < 0.01$ ,  $***p < 0.001$ , and  $****p < 0.0001$ .

### RESOURCE AVAILABILITY

#### Lead contact

Further information and requests for resources should be directed to and will be fulfilled by the lead contact, Zhou Li ([zli@binn.cas.cn](mailto:zli@binn.cas.cn)).

#### Materials availability

This study did not generate new unique reagents.

#### Data and code availability

The data supporting the findings in this study are available within the paper and its supplemental information. All data generated in this study are available from the corresponding author upon reasonable request. Source data are provided with this paper. This paper does not report original code.

### ACKNOWLEDGMENTS

We greatly acknowledge financial support from National Natural Science Foundation of China T2125003 (to Z.L.), 22027810 (to C.C.), 22388101 (to C.C.), and 52373256 (to H.O.); Beijing Natural Science Foundation L245015 (to Z.L.) and 7232347 (to H.O.); National Key Research and Development Program of China 2022YFE0111700 (to Z.L.) and 2021YFA1200900 (to C.C.); New Cornerstone Science Foundation (to C.C.); Youth Innovation Promotion Association CAS 2023176 (to H.O.); Fundamental Research Funds for the Central Universities E0EG6802X2 (to Z.L.) and E2E45101X2 (to H.O.); Beijing Nova Program 2024047 (to H.O.); and Tianjin Science and Technology Planning Project 21ZXJBSY00120 (to D.F.). The authors appreciate the members of the UCAS, NCNST, and BINN research facilities for their help with microfabrication/characterization. We are grateful to Prof. Xia Wang (SICNU) and other laboratory members for their cooperation and advice in this study.

### AUTHOR CONTRIBUTIONS

L.X., E.W., Y.K., and D.F. contributed equally. H.O., L.X., and E.W. conceived and designed the experiments. L.X., E.W., Y.K., and D.F. performed the experiments. E.W. fabricated and characterized the high-voltage generator. L.X., E.W., Y.K., and D.F. performed the cell and animal experiments. J.Z. assisted

with the rabbit ablation experiment. L.X., E.W., and H.O. analyzed the data. L.L., Y.Q., J.H., X.C., and Y.X. contributed materials and analysis tools. Z.L. and C.C. supervised the project. L.X. and E.W. wrote the paper. H.O., Z.L., and C.C. revised the paper. All authors critically reviewed and approved the paper.

### DECLARATION OF INTERESTS

The authors declare that they have no competing interests.

### SUPPLEMENTAL INFORMATION

Supplemental information can be found online at <https://doi.org/10.1016/j.device.2025.100721>.

Received: October 25, 2024

Revised: January 20, 2025

Accepted: February 3, 2025

Published: March 3, 2025

### REFERENCES

- Ruiz-Fernández, A.R., Campos, L., Gutierrez-Maldonado, S.E., Nunez, G., Villanelo, F., and Perez-Acle, T. (2022). Nanosecond pulsed electric field (nspef): Opening the biotechnological pandora's box. *Int. J. Mol. Sci.* 23, 6158. <https://doi.org/10.3390/ijms23116158>.
- Stacey, M., Fox, P., Buescher, S., and Kolb, J. (2011). Nanosecond pulsed electric field induced cytoskeleton, nuclear membrane and telomere damage adversely impact cell survival. *Bioelectrochemistry* 82, 131–134. <https://doi.org/10.1016/j.bioelechem.2011.06.002>.
- Ruiz-Fernández, A.R., Roseblatt, M., and Perez-Acle, T. (2022). Nanosecond pulsed electric field (nsPEF) and vaccines: a novel technique for the inactivation of SARS-CoV-2 and other viruses? *Ann. Med.* 54, 1749–1756. <https://doi.org/10.1080/07853890.2022.2087898>.
- Wang, T., and Xie, X. (2023). Nanosecond bacteria inactivation realized by locally enhanced electric field treatment. *Nat. Water* 1, 104–112. <https://doi.org/10.1038/s44221-022-00003-2>.
- Sinha, S.K., Khammari, A., Picher, M., Roulland, F., Viart, N., LaGrange, T., and Banhart, F. (2019). Nanosecond electron pulses in the analytical electron microscopy of a fast irreversible chemical reaction. *Nat. Commun.* 10, 3648. <https://doi.org/10.1038/s41467-019-11669-w>.
- Ahmad, V., Sobus, J., Greenberg, M., Shukla, A., Philippa, B., Pivrikas, A., Vamvounis, G., White, R., Lo, S.C., Namdas, E.B., et al. (2020). Charge and exciton dynamics of oleds under high voltage nanosecond pulse: Towards injection lasing. *Nat. Commun.* 11, 4310. <https://doi.org/10.1038/s41467-020-18094-4>.
- Yan, J., Shen, S., and Ding, W. (2020). High-power nanosecond pulse generators with improved reliability by adopting auxiliary triggering topology. *IEEE Trans. Power Electron.* 35, 1353–1364. <https://doi.org/10.1109/tpel.2019.2922360>.
- Shen, S., Yan, J., Sun, G., and Ding, W. (2021). Improved auxiliary triggering topology for high-power nanosecond pulse generators based on avalanche transistors. *IEEE Trans. Power Electron.* 36, 13634–13644. <https://doi.org/10.1109/tpel.2021.3087732>.
- Dwyer, J.R., and Uman, M.A. (2014). The physics of lightning. *Phys. Rep.* 534, 147–241. <https://doi.org/10.1016/j.physrep.2013.09.004>.
- Wang, Y., Yamada, N., Xu, J., Zhang, J., Chen, Q., Ootani, Y., Higuchi, Y., Ozawa, N., Bouchet, M.I.D.B., Martin, J.M., et al. (2019). Triboemission of hydrocarbon molecules from diamond-like carbon friction interface induces atomic-scale wear. *Sci. Adv.* 5, eaax9301. <https://doi.org/10.1126/sciadv.aax9301>.
- Cheng, J., Ding, W., Zi, Y., Lu, Y., Ji, L., Liu, F., Wu, C., and Wang, Z.L. (2018). Triboelectric microplasma powered by mechanical stimuli. *Nat. Commun.* 9, 3733. <https://doi.org/10.1038/s41467-018-06198-x>.

12. Liu, C., Wang, F., and Du, X. (2024). Self-powered electrostatic tweezer for adaptive object manipulation. *Device* 2, 100465. <https://doi.org/10.1016/j.device.2024.100465>.
13. Wang, Z.L., and Wang, A.C. (2019). On the origin of contact-electrification. *Mater. Today* 30, 34–51. <https://doi.org/10.1016/j.mattod.2019.05.016>.
14. Ock, I.W., Yin, J., Wang, S., Zhao, X., Baik, J.M., and Chen, J. (2024). Advances in Blue Energy Fuels: Harvesting Energy from Ocean for Self-Powered Electrolysis. *Adv. Energy Mater.* 15, 2400563. <https://doi.org/10.1002/aenm.202400563>.
15. Conta, G., Libanori, A., Tat, T., Chen, G., and Chen, J. (2021). Triboelectric Nanogenerators for Therapeutic Electrical Stimulation. *Adv. Mater.* 33, 2007502. <https://doi.org/10.1002/adma.202007502>.
16. Liu, D., Gao, Y., Zhou, L., Wang, J., and Wang, Z.L. (2023). Recent advances in high-performance triboelectric nanogenerators. *Nano Res.* 16, 11698–11717. <https://doi.org/10.1007/s12274-023-5660-8>.
17. Zhang, S., Bick, M., Xiao, X., Chen, G., Nashalian, A., and Chen, J. (2021). Leveraging triboelectric nanogenerators for bioengineering. *Matter* 4, 845–887. <https://doi.org/10.1016/j.matt.2021.01.006>.
18. Zhou, Z., Chen, K., Li, X., Zhang, S., Wu, Y., Zhou, Y., Meng, K., Sun, C., He, Q., Fan, W., et al. (2020). Sign-to-speech translation using machine-learning-assisted stretchable sensor arrays. *Nat. Electron.* 3, 571–578. <https://doi.org/10.1038/s41928-020-0428-6>.
19. Hinchet, R., Yoon, H.J., Ryu, H., Kim, M.K., Choi, E.K., Kim, D.S., and Kim, S.W. (2019). Transcutaneous ultrasound energy harvesting using capacitive triboelectric technology. *Science* 365, 491–494. <https://doi.org/10.1126/science.aan3997>.
20. Qu, X., Liu, Z., Tan, P., Wang, C., Liu, Y., Feng, H., Luo, D., Li, Z., and Wang, Z.L. (2022). Artificial tactile perception smart finger for material identification based on triboelectric sensing. *Sci. Adv.* 8, eabq2521. <https://doi.org/10.1126/sciadv.abq2521>.
21. Shen, S., Zhou, Q., Chen, G., Fang, Y., Kurilova, O., Liu, Z., Li, S., and Chen, J. (2024). Advances in wearable respiration sensors. *Psychol. Res. Behav. Manag.* 72, 140–162. <https://doi.org/10.1016/j.mattod.2023.12.003>.
22. Li, S., Zhao, K., Zan, G., Kim, G., Oh, J., Jiang, W., Shin, E., Kim, W., Kim, T., Jang, J., et al. (2024). A biodegradable silk-based energy-generating skin with dual-mode tactile perception. *Device* 3, 100561. <https://doi.org/10.1016/j.device.2024.100561>.
23. Bai, Y., Chen, S., Wang, H., Wang, E., Kong, X., Gai, Y., Qu, X., Li, Q., Xue, S., Guo, P., et al. (2022). Chemical warfare agents decontamination via air microplasma excited by a triboelectric nanogenerator. *Nano Energy* 95, 106992. <https://doi.org/10.1016/j.nanoen.2022.106992>.
24. Liu, Z., Hu, Y., Qu, X., Liu, Y., Cheng, S., Zhang, Z., Shan, Y., Luo, R., Weng, S., Li, H., et al. (2024). A self-powered intracardiac pacemaker in swine model. *Nat. Commun.* 15, 507. <https://doi.org/10.1038/s41467-023-44510-6>.
25. Cheng, T., Shao, J., and Wang, Z.L. (2023). Triboelectric nanogenerators. *Nat. Rev. Methods Primers* 3, 39. <https://doi.org/10.1038/s43586-023-00220-3>.
26. Wu, C., Wang, A.C., Ding, W., Guo, H., and Wang, Z.L. (2018). Triboelectric nanogenerator: A foundation of the energy for the new era. *Adv. Energy Mater.* 9, 1802906. <https://doi.org/10.1002/aenm.201802906>.
27. Cheng, X., Tang, W., Song, Y., Chen, H., Zhang, H., and Wang, Z.L. (2019). Power management and effective energy storage of pulsed output from triboelectric nanogenerator. *Nano Energy* 61, 517–532. <https://doi.org/10.1016/j.nanoen.2019.04.096>.
28. Yi, F., Wang, X., Niu, S., Li, S., Yin, Y., Dai, K., Zhang, G., Lin, L., Wen, Z., Guo, H., et al. (2016). A highly shape-adaptive, stretchable design based on conductive liquid for energy harvesting and self-powered biomechanical monitoring. *Sci. Adv.* 2, e1501624. <https://doi.org/10.1126/sciadv.1501624>.
29. Zhang, Z., Wang, Z., Chen, Y., Feng, Y., Dong, S., Zhou, H., Wang, Z.L., and Zhang, C. (2022). Semiconductor contact-electrification-dominated tribovoltaic effect for ultrahigh power generation. *Adv. Mater.* 34, e2200146. <https://doi.org/10.1002/adma.202200146>.
30. Zhang, Z., Gong, L., Luan, R., Feng, Y., Cao, J., and Zhang, C. (2024). Tribovoltaic effect: Origin, interface, characteristic, mechanism & application. *Adv. Sci.* 11, e2305460. <https://doi.org/10.1002/advs.202305460>.
31. Liu, D., Yin, X., Guo, H., Zhou, L., Li, X., Zhang, C., Wang, J., and Wang, Z.L. (2019). A constant current triboelectric nanogenerator arising from electrostatic breakdown. *Sci. Adv.* 5, eaav6437. <https://doi.org/10.1126/sciadv.aav6437>.
32. Nuccitelli, R. (2019). Application of pulsed electric fields to cancer therapy. *Bioelectricity* 1, 30–34. <https://doi.org/10.1089/bioe.2018.0001>.
33. Guo, S., Burcus, N.I., Hornef, J., Jing, Y., Jiang, C., Heller, R., and Beebe, S.J. (2018). Nano-pulse stimulation for the treatment of pancreatic cancer and the changes in immune profile. *Cancers* 10, 217. <https://doi.org/10.3390/cancers10070217>.
34. Guo, S., Jing, Y., Burcus, N.I., Lassiter, B.P., Tanaz, R., Heller, R., and Beebe, S.J. (2018). Nano-pulse stimulation induces potent immune responses, eradicating local breast cancer while reducing distant metastases. *Int. J. Cancer* 142, 629–640. <https://doi.org/10.1002/ijc.31071>.
35. Xu, M., Xu, D., Dong, G., Ren, Z., Zhang, W., Aji, T., Zhao, Q., Chen, X., and Jiang, T. (2022). The safety and efficacy of nanosecond pulsed electric field in patients with hepatocellular carcinoma: A prospective phase 1 clinical study protocol. *Front. Oncol.* 12, 869316. <https://doi.org/10.3389/fonc.2022.869316>.
36. Liu, H., Yao, C., Zhao, Y., Chen, X., Dong, S., Wang, L., and Davalos, R.V. (2021). In vitro experimental and numerical studies on the preferential ablation of chemo-resistant tumor cells induced by high-voltage nanosecond pulsed electric fields. *IEEE Trans. Biomed. Eng.* 68, 2400–2411. <https://doi.org/10.1109/tbme.2020.3040337>.
37. Krysko, D.V., Garg, A.D., Kaczmarek, A., Krysko, O., Agostinis, P., and Vandenabeele, P. (2012). Immunogenic cell death and dams in cancer therapy. *Nat. Rev. Cancer* 12, 860–875. <https://doi.org/10.1038/nrc3380>.
38. Kielbik, A., Szlasa, W., Novickij, V., Szewczyk, A., Maciejewska, M., Saczko, J., and Kulbacka, J. (2021). Effects of high-frequency nanosecond pulses on prostate cancer cells. *Sci. Rep.* 11, 15835. <https://doi.org/10.1038/s41598-021-95180-7>.
39. Wang, J., Sun, Z., Hu, G., Ding, H., and Li, X. (2024). Improving mechanical energy harvesters without complex fabrication using origami/kirigami. *Device* 2, 100548. <https://doi.org/10.1016/j.device.2024.100548>.
40. Guo, J., Yang, X., Xie, Y., Zheng, J., Lin, W., Liao, J., Huang, H., Duan, J., Yang, P., Tang, Q., and Wang, Z.L. (2025). Boosting the power conversion efficiency of hybrid triboelectric-photovoltaic cells through the field coupling effect. *Device* 3, 100562. <https://doi.org/10.1016/j.device.2024.100562>.
41. Zhang, H., Chen, Y., Deng, L., Zhu, X., Xu, C., Xie, L., Yang, Q., and Zhang, H. (2024). Efficient electrical energy conversion strategies from triboelectric nanogenerators to practical applications: A review. *Nano Energy* 132, 110383. <https://doi.org/10.1016/j.nanoen.2024.110383>.
42. Park, Y.J., Ro, Y.G., Shin, Y.E., Park, C., Na, S., Chang, Y., and Ko, H. (2023). Multi-Layered Triboelectric Nanogenerators with Controllable Multiple Spikes for Low-Power Artificial Synaptic Devices. *Adv. Sci.* 10, e2304598. <https://doi.org/10.1002/advs.202304598>.